Wave reflection at an anelastic transversely isotropic ocean bottom

Rolf Sidler[1] and José M. Carcione[1]

ABSTRACT

We study the reflection of waves at the ocean bottom, which is modeled as a plane interface separating a viscoacoustic medium (water) and a viscoelastic transversely isotropic solid whose axis of rotational symmetry is perpendicular to the bottom. We compute the plane-wave reflection coefficient (including the phenomenon known as the Rayleigh window) both numerically — by amplitude variation with offset (AVO) analysis of synthetic seismograms generated using a domain decomposition method and analytically. A first simulation considers the water-steel interface, for which experimental data is available. Then, we consider soft sediments and stiff crustal rocks for various values of the anellipticity parameter δ. The domain-decomposition technique relies on one grid for the fluid and another grid for the solid and uses Fourier and Chebyshev differential operators. The anelastic and anisotropic stress-strain relation is described by the Zener model. Special attention is given to modeling the boundary conditions at the ocean bottom. For this purpose, we further develop the technique for wave propagation at fluid/anelastic-anisotropic-solid interfaces. AVO slowness-frequency-domain analysis is used to compute the reflection coefficient and phase angle from the synthetic seismograms. This allows us to verify the domain-decomposition algorithm, which is shown to model with high accuracy the Rayleigh window for varying δ. The comparison also verifies the calculation of the analytical plane-wave reflection coefficient because a wrong choice of the sign of the vertical slowness of the reflected wave may cause nonphysical discontinuities in the coefficient. Moreover, the pseudospectral modeling code allows a general material variability and a complete and accurate characterization of the seismic response of an anisotropic ocean bottom.

INTRODUCTION

The problem of reflection, refraction, and propagation at a plane boundary separating a viscoacoustic medium (lossy fluid) and a viscoelastic anisotropic solid has practical application in seismic exploration, seismology, foundation engineering, and nondestructive testing of materials. The ocean-bottom interface may separate the water column from a finely layered formation whose strata are parallel to the interface. In this case, the formation can be replaced by a homogeneous transversely isotropic (TI) medium whose symmetry axis is perpendicular to the bottom. This situation occurs when the wavelength of the seismic pulse is much larger than the thickness of the single layers (Postma, 1955).

In seismic exploration, the characterization of the ocean bottom is useful for data processing of multicomponent seismic surveys acquired at the seafloor. Knowledge of S-wave velocities is required for static corrections and imaging of mode-converted PS-waves. Shear velocity is also important for multiple removal and amplitude variation with offset (AVO) analysis.

To our knowledge, the viscoelastic problem has been addressed only in the isotropic case. In the case of isotropic porous media, the problem is somewhat similar because of the presence of a viscous fluid within the pores (e.g., Wu et al., 1990; Santos et al., 1992; Denneman et al., 2002). Borcherdt et al. (1986) present theoretical and experimental results corresponding to a water-steel interface, where the phenomenon called the Rayleigh window occurs. This viscoelastic effect implies that the energy incident on the boundary at angles within that window is substantially transmitted.

The phenomenon is associated with the presence of inhomogeneous body waves, only present in anelastic media. It cannot be predicted by using reflection coefficients based on the elasticity theory (Brekhovskikh, 1960, p. 34). The amplitude of minimum reflection depends on the shear-wave loss, whereas the position of the window depends mainly on the shear-wave velocity. These two effects are largely independent. Moreover, the effect is important for hard ocean bottoms when the crustal shear velocity is greater than that of the incident P-wave. The problem has been investigated further by

Carcione and Helle (2004) and Carcione (2006) using numerical simulation.

In this article, we propose a new domain-decomposition technique for a fluid/TI solid interface to model the ocean-bottom boundary conditions accurately. There exists no analytical solution for this problem. Therefore, the domain-decomposition-based algorithm is a novel tool for computing the response of the ocean bottom in the presence of anisotropy. A similar simulation algorithm, based on a domain-decomposition method to model wave propagation through a crack in a TI medium, is given by Carcione (1998).

We also show how to compute the reflection coefficient analytically. The analytical result serves as a cross-check of the domain-decomposition algorithms. However, the choice of the correct sign of the vertical slowness of the various waves is essential; otherwise, nonphysical discontinuities may appear. As indicated by Krebes (1984), special care is needed when choosing that sign because a wrong choice may lead to discontinuities of the vertical slowness as a function of the incidence angle.

Unlike the elastic case, the amplitude of the scattered waves can grow exponentially with distance from the interface (Richards, 1984). Thus, the condition of an exponentially decaying wave is not sufficient to obtain the reflection and transmission coefficients. Instead, the signs of the real and imaginary parts of the vertical slowness should be chosen to guarantee a smooth variation as a function of the incidence angle.

This problem has been studied by Ruud (2006), who analyzes the different criteria to obtain the sign of the vertical slowness as a function of the incidence angle. Ruud (2006) concludes that the energy-velocity vector criterion should be used for subcritical angles and the radiation condition should be used for supercritical angles. Nevertheless, the problem remains because these conditions must be verified further, and the nature of critical angle in anelastic media is unclear.

The comparison between the plane-wave theory and the numerical calculations serves as a cross-check of the modeling algorithm, where we use an AVO inversion method to obtain the numerical plane-wave reflection coefficient. The cross-check also solves for ambiguities in calculating the reflection coefficients on account of the choice of the sign of the vertical slowness when computing the analytical plane-wave reflection coefficient.

The novel aspects of this work compared to that of Carcione and Helle (2004) are: (1) the use of a viscoelastic TI stress-strain relation for the ocean bottom, (2) the generalization of the domain-decomposition technique to the TI case, (3) the generalization of the analytical plane-wave reflection coefficient to the TI case, and (4) the analysis of the behavior of the Rayleigh window for anisotropic media.

THE ELASTIC CONSTANTS

Without loss of generality, we consider the 2D qP-qSV case, where the relevant elastic constants in the (x, z) propagation plane are c_{11}, c_{33}, c_{13}, and c_{55}. These constants correspond to the unrelaxed (high-frequency) limit. We define $c_{11} \equiv \rho v_P^2$ and $c_{55} \equiv \rho v_S^2$, where ρ is the density and v_P and v_S are P- and S-wave velocities. The isotropic limit implies $c_{11} = c_{33}$ and $c_{13} = c_{11} - 2c_{55}$.

We quantify the degree anisotropy with

$$\epsilon = \frac{c_{11} - c_{33}}{2c_{33}} \tag{1}$$

and the anellipticity parameter δ:

$$\delta = \frac{(c_{13} + c_{55})^2 - (c_{33} - c_{55})^2}{2c_{33}(c_{33} - c_{55})} \tag{2}$$

(Thomsen, 1986). Although ϵ is related to the fractional difference between the horizontal and vertical P-wave velocity, δ is responsible for the angular dependence of the P-wave velocity in the vicinity of the vertical direction. The P-wave velocity increases away from the vertical if δ is positive and decreases if δ is negative (Tsvankin, 2005). In the isotropic case, $\epsilon = \delta = 0$.

Given c_{11}, c_{33}, c_{55}, and δ, we obtain

$$c_{13} = \sqrt{2\delta c_{33}(c_{33} - c_{55}) + (c_{33} - c_{55})^2} - c_{55}. \tag{3}$$

Thus, varying δ means changing c_{13}. In general, when we vary ϵ, we keep constant c_{11} and vary $c_{33} = c_{11}/(1 + 2\epsilon)$. Otherwise, we keep constant c_{33} and obtain $c_{11} = (1 + 2\epsilon)c_{33}$. If $c_{11} = c_{33}$ (cubic symmetry), δ is the only parameter quantifying the anisotropy.

MODELING EQUATIONS

The reference work is Carcione and Helle (2004), where the isotropic case is considered. Here, we extend the stress-strain relation to the TI case, with the symmetry axis perpendicular to the fluid-solid interface. The qP-qSV equations of motion are given by (Carcione, 2001) the following.

Euler's equations

$$\partial_x \sigma_{xx} + \partial_z \sigma_{xz} = \rho \partial_t v_x, \tag{4}$$

$$\partial_x \sigma_{xz} + \partial_z \sigma_{zz} = \rho \partial_t v_z, \tag{5}$$

where v and σ denote particle velocity and stress, and ρ is the density.

Stress-strain relations

$$\partial_t \sigma_{xx} = c_{11}\partial_x v_x + c_{13}\partial_z v_z + \bar{\mathcal{K}}e_1 + 2c_{55}e_2, \tag{6}$$

$$\partial_t \sigma_{zz} = c_{13}\partial_x v_x + c_{33}\partial_z v_z + \bar{\mathcal{K}}e_1 - 2c_{55}e_2, \tag{7}$$

$$\partial_t \sigma_{xz} = c_{55}(\partial_z v_x + \partial_x v_z + e_3), \tag{8}$$

where e_1, e_2, and e_3 are memory variables and

$$\bar{\mathcal{K}} = \bar{\mathcal{E}} - c_{55}, \quad \bar{\mathcal{E}} = \frac{1}{2}(c_{11} + c_{33}). \tag{9}$$

Memory-variable equations

$$\partial_t e_1 = \frac{1}{\tau_\sigma^{(1)}}\left[\left(\frac{\tau_\sigma^{(1)}}{\tau_\epsilon^{(1)}} - 1\right)(\partial_x v_x + \partial_z v_z) - e_1\right], \tag{10}$$

$$\partial_t e_2 = \frac{1}{2\tau_\sigma^{(2)}}\left[\left(\frac{\tau_\sigma^{(2)}}{\tau_\epsilon^{(2)}} - 1\right)(\partial_x v_x - \partial_z v_z) - 2e_2\right], \tag{11}$$

$$\partial_t e_3 = \frac{1}{\tau_\sigma^{(2)}}\left[\left(\frac{\tau_\sigma^{(2)}}{\tau_\epsilon^{(2)}} - 1\right)(\partial_z v_x + \partial_x v_z) - e_3\right], \tag{12}$$

where $\tau_\sigma^{(\nu)}$ and $\tau_\epsilon^{(\nu)}$ are relaxation times related to dilatational ($\nu = 1$) and shear ($\nu = 2$) deformations. The frequency-domain stress-strain relations are obtained from the preceding equations by applying the Fourier transform (see Appendix A). The stress-strain relations satisfy the condition that the mean stress depends only on the dilatational relaxation function in any coordinate system; the trace of the stress tensor should be invariant under coordinate transformations. Moreover, the deviatoric stresses solely depend on the shear relaxation function (see Carcione, 2001).

The equations for the fluid (viscoacoustic medium) are obtained from equations 4–12 as a limiting case. The equations of motion read

$$\rho \partial_t v_x = \partial_x \sigma, \tag{13}$$

$$\rho \partial_t v_z = \partial_z \sigma, \tag{14}$$

where

$$\partial_t \sigma = \lambda(v_{x,x} + v_{z,z} + e_1) + s_f, \tag{15}$$

together with the memory-variable equation 10, where λ is the bulk modulus and s_f is the source.

MODELING ALGORITHM AND DOMAIN DECOMPOSITION

The numerical solution is obtained by generalizing to the anisotropic case the algorithm used by Carcione and Helle (2004). The boundary conditions at the ocean bottom require the continuity of the normal particle velocity v_z and stress component σ_{zz}, where $\sigma_{xz} = 0$ (e.g., Carcione, 2001).

Two grids model the fluid and solid subdomains. The solution on each grid is obtained by using the Runge-Kutta method as a time-stepping algorithm and the Fourier and Chebyshev differential operators to compute the spatial derivatives in the horizontal and vertical directions, respectively (Carcione and Helle, 2004). To combine the two grids (domain decomposition), the wavefield is decomposed into incoming and outgoing wave modes at the interface between the solid and the fluid.

The inward-propagating waves depend on the solution exterior to the subdomains and therefore are computed from the boundary conditions. The behavior of the outward-propagating waves is determined by the solution inside the subdomain. The approach is adapted here for the anisotropic case and involves the equations given for updating the field variables at the grid points defining the fluid-solid interface.

The fluid is denoted by the subscript 1 and the solid by the subscript 2. The symbol P indicates the compressional wave in the fluid or the qP-wave in solid, and S denotes the qS-wave in this medium. The boundary equations at the fluid-solid interface are generalizations to the TI case (the interface perpendicular to the symmetry axis) of the equations given in Carcione and Helle (2004):

$$v_x^{\text{new}}(1) = v_x^{\text{old}}(1),$$

$$v_z^{\text{new}} = [Z_P(1) + Z_P(2)]^{-1}[Z_P(2)v_z^{\text{old}}(2) + Z_P(1)v_z^{\text{old}}(1) + \sigma^{\text{old}}(1) - \sigma_{zz}^{\text{old}}(2)],$$

$$\sigma^{\text{new}} = \sigma_{zz}^{\text{new}} = \frac{Z_P(1)Z_P(2)}{Z_P(1) + Z_P(2)}\left[v_z^{\text{old}}(1) - v_z^{\text{old}}(2) + \frac{\sigma^{\text{old}}(1)}{Z_P(1)} + \frac{\sigma_{zz}^{\text{old}}(2)}{Z_P(2)}\right],$$

$$e_1^{\text{new}}(1) = e_1^{\text{old}}(1) + \frac{\phi_1(1)}{\lambda}[\sigma^{\text{new}} - \sigma^{\text{old}}(1)],$$

$$v_x^{\text{new}}(2) = v_x^{\text{old}}(2) - \sigma_{xz}^{\text{old}}(2)/Z_S(2),$$

$$\sigma_{xz}^{\text{new}}(2) = 0,$$

$$\sigma_{xx}^{\text{new}}(2) = \sigma_{xx}^{\text{old}}(2) + \frac{c_{13}}{c_{33}}[\sigma_{zz}^{\text{new}} - \sigma_{zz}^{\text{old}}(2)],$$

$$e_1^{\text{new}}(2) = e_1^{\text{old}}(2) + \frac{\phi_1(2)}{c_{33}}[\sigma_{zz}^{\text{new}} - \sigma_{zz}^{\text{old}}(2)],$$

$$e_2^{\text{new}}(2) = e_2^{\text{old}}(2) - \frac{\phi_2(2)}{c_{33}}[\sigma_{zz}^{\text{new}} - \sigma_{zz}^{\text{old}}(2)],$$

$$e_3^{\text{new}}(2) = e_3^{\text{old}}(2) - \frac{\phi_2(2)}{c_{55}}\sigma_{xz}^{\text{old}}(2), \tag{16}$$

where $\phi_\nu = 1/\tau_\sigma^{(\nu)} - 1/\tau_\epsilon^{(\nu)}$, $Z_P(1) = \sqrt{\rho_1 \lambda}$, $Z_P(2) = \sqrt{\rho_2 c_{33}}$, and $Z_S(2) = \sqrt{\rho_2 c_{55}}$.

These equations indicate how the wavefield at the boundary grid points must be updated (new) as a function of the previous values (old) at each time step.

The upper boundary of subdomain 1 (the fluid) satisfies the nonreflecting conditions:

$$v_z^{\text{new}} = \frac{1}{2}\left(v_z^{\text{old}} - \frac{\sigma^{\text{old}}}{Z_P}\right),$$

$$\sigma^{\text{new}} = \frac{1}{2}(\sigma^{\text{old}} - Z_P v_z^{\text{old}}),$$

$$e_1^{\text{new}} = e_1^{\text{old}} - \frac{\phi_1}{(2\lambda)}(\sigma^{\text{old}} + Z_P v_z^{\text{old}}). \tag{17}$$

The lower boundary of subdomain 2 (the solid) satisfies the nonreflecting conditions:

$$v_x^{\text{new}} = \frac{1}{2}(v_x^{\text{old}} + \sigma_{xz}^{\text{old}}/Z_S),$$

$$v_z^{\text{new}} = \frac{1}{2}(v_z^{\text{old}} + \sigma_{zz}^{\text{old}}/Z_P),$$

$$\sigma_{xx}^{\text{new}} = \sigma_{xx}^{\text{old}} - (c_{13}/(2c_{33}))(\sigma_{zz}^{\text{old}} - Z_P v_z^{\text{old}}),$$

$$\sigma_{zz}^{\text{new}} = \frac{1}{2}(\sigma_{zz}^{\text{old}} + Z_P v_z^{\text{old}}),$$

$$\sigma_{xz}^{\text{new}} = \frac{1}{2}(\sigma_{xz}^{\text{old}} + Z_S v_x^{\text{old}}),$$

$$e_1^{\text{new}} = e_1^{\text{old}} - \frac{\phi_1}{(2c_{33})}(\sigma_{zz}^{\text{old}} - Z_P v_z^{\text{old}}),$$

$$e_2^{\text{new}} = e_2^{\text{old}} + \frac{\phi_2}{(2c_{33})}(\sigma_{zz}^{\text{old}} - Z_P v_z^{\text{old}}),$$

$$e_3^{\text{new}} = e_3^{\text{old}} - \frac{\phi_2}{(2c_{55})}(\sigma_{xz}^{\text{old}} - Z_S v_x^{\text{old}}). \quad (18)$$

In addition to the nonreflecting conditions, absorbing strips are used to further attenuate the wave field at nonphysical boundaries (Carcione and Helle, 2004).

ANALYTICAL PLANE-WAVE REFLECTION COEFFICIENTS

The expression of the reflection and transmission coefficients are a generalization of equations 6.187–6.193 in Carcione (2001) to the TI case. R_{PP}, T_{PP}, and T_{PS} denote the reflection and transmission coefficient of the compressional and the compressional-to-shear converted wave, respectively. The boundary conditions require continuity of

$$v_z, \quad \sigma_{zz}, \quad \text{and} \quad \sigma_{xz} = 0. \quad (19)$$

These conditions generate the following matrix equation for the reflection and transmission coefficients:

$$\begin{pmatrix} \xi_{P_1} & \xi_{P_2} & \xi_{S_2} \\ Z_{P_1} & -Z_{P_2} & -Z_{S_2} \\ 0 & W_{P_2} & W_{S_2} \end{pmatrix} \begin{pmatrix} R_{PP} \\ T_{PP} \\ T_{PS} \end{pmatrix} = \begin{pmatrix} \xi_{P_1} \\ -Z_{P_1} \\ 0 \end{pmatrix}, \quad (20)$$

where

$$Z_{P_1} = ps = \sqrt{\rho p}, \quad p = \lambda M(\omega), \quad s = \sqrt{\rho/p},$$

$$W_{P_2} = p_{55}(\xi_{P_2}s_x + \beta_{P_2}s_{z_{P_2}}),$$

$$Z_{P_2} = \beta_{P_2}p_{13}s_x + \xi_{P_2}p_{33}s_{z_{P_2}},$$

$$W_{S_2} = p_{55}(\xi_{S_2}s_x + \beta_{S_2}s_{z_{S_2}}),$$

$$Z_{S_2} = \beta_{S_2}p_{13}s_x + \xi_{S_2}p_{33}s_{z_{S_2}}, \quad (21)$$

with the relaxed material constants p_{ij} and the complex modulus of the fluid M having the form of equations A-2 and A-3.

The horizontal slowness is the same for all of the waves (Snell's law) and is given by

$$s_x = \sin\theta\sqrt{\frac{\rho}{p}}, \quad (22)$$

where θ is the incidence propagation angle and ρ is the fluid density.

The polarization components for the fluid are

$$\beta_{P_1} = \frac{s_x}{s}, \quad \xi_{P_1} = \frac{s_z}{s}, \quad s_z = \text{pv}\sqrt{s^2 - s_x^2}, \quad (23)$$

where pv denotes the principal value. (For the principal value, the argument of the square root lies between $-\pi/2$ and $+\pi/2$).

The vertical slownesses $s_{z_{P_2}}$ and $s_{z_{S_2}}$ are computed as

$$s_z = \pm\frac{1}{\sqrt{2}}\sqrt{K_1 \mp \text{pv}\sqrt{K_1^2 - 4K_2K_3}}, \quad (24)$$

where

$$K_1 = \rho\left(\frac{1}{p_{55}} + \frac{1}{p_{33}}\right) + \frac{1}{p_{55}}\left[\frac{p_{13}}{p_{33}}(p_{13} + 2p_{55}) - p_{11}\right]s_x^2,$$

$$K_2 = \frac{1}{p_{33}}(p_{11}s_x^2 - \rho), \quad K_3 = s_x^2 - \frac{\rho}{p_{55}}.$$

If the z-axis points downward, the signs in s_z correspond to

$$(+ , -) \quad \text{downward-propagating qP-wave,}$$
$$(+ , +) \quad \text{downward-propagating qS-wave,}$$
$$(- , -) \quad \text{upward-propagating qP-wave,}$$
$$(- , +) \quad \text{upward-propagating qS-wave.}$$

An incorrect choice may cause nonphysical discontinuities in the reflection coefficients.

The polarization components for the solid are

$$\beta = \text{pv}\sqrt{\frac{p_{55}s_x^2 + p_{33}s_z^2 - \rho}{p_{11}s_x^2 + p_{33}s_z^2 + p_{55}(s_x^2 + s_z^2) - 2\rho}} \quad (25)$$

and

$$\xi = \pm\text{pv}\sqrt{\frac{p_{11}s_x^2 + p_{55}s_z^2 - \rho}{p_{11}s_x^2 + p_{33}s_z^2 + p_{55}(s_x^2 + s_z^2) - 2\rho}}, \quad (26)$$

respectively. In general, the plus and minus signs correspond to the qP- and qS-waves, respectively; however, one must choose the signs such that ξ varies smoothly with the propagation angle.

NUMERICAL PLANE-WAVE REFLECTION COEFFICIENTS: AVO METHOD

To compute the PP reflection coefficient versus incidence angle from the synthetic seismograms obtained with the domain-decomposition modeling, we use the AVO inversion technique applied by Carcione and Helle (2004) to an isotropic and viscoelastic ocean-bottom interface. Denoting frequency and horizontal slowness by $f = \omega/(2\pi)$ and s_x, respectively, the method consists of the following steps.

1) Generate a synthetic seismogram of the pressure field σ, placing a line of receivers at each grid point above the interface. This record contains the incident and reflected fields.
2) Compute the synthetic seismogram without interface at the same location (set the properties of the lower medium to those of the upper medium). The seismogram contains the incident field only.
3) Perform the difference between the first and second seismograms. The difference contains the reflected field only.
4) Perform an (f, s_x) transform of the incident field to obtain $\sigma_I(f, s_x)$.
5) Perform an (f, s_x) transform of the reflected field to obtain $\sigma_R(f, s_x)$.

6) The ratio $|\sigma_R(f,s_x)|/|\sigma_I(f,s_x)|$ is the reflection coefficient, and the phase angle is given by $\arctan[\sigma_R(f,s_x)/\sigma_I(f,s_x)]$. Transform s_x to incidence angle by using $\sin\theta = v_{P_1}s_x$, where v_{P_1} is the sound velocity in the upper medium.

EXAMPLES

First, we show the type of nonphysical discontinuity to be expected in the reflection coefficient when the wrong sign in the vertical slowness equation 24 is chosen. In this case, and in all the examples shown in this article, the frequency is chosen as the center frequency of the relaxation peaks, i.e., $\omega = 1/\tau_0$. The properties of water are taken as $\lambda = 2.25$ GPa, $\rho = 1040$ kg/m^3, and $Q = 10,000$. The properties of the solid are $v_P = 4323$ m/s, $v_S = 1449$ m/s, $\delta = 0.1$, $\rho = 2760$ kg/m^3, $Q_1 = 40$, and $Q_2 = 100$.

Figure 1 shows the reflection coefficient as a function of the incidence angle. The solid line is the correct coefficient, and the dashed line corresponds to the wrong sign, which causes a discontinuity at nearly 50°. The symbols represent the numerical calculation applying the AVO method to the synthetic seismograms at different frequencies. The mesh for the fluid has 375×81 points, and the mesh of the solid has 375×41 points. The horizontal grid spacing is 5 m for both meshes, and the vertical size of each grid is 260 m. The source, a Ricker wavelet located 138 m above the interface with a dominant frequency of 35 Hz, is the same as the central frequency of the relaxation peaks. The time step of the Runge-Kutta method is 50 μs.

The theoretical and numerical phase angles mismatch because the receivers are located at the penultimate grid row of the upper grid, above the interface. Then, there is a phase shift between the incident wave and the reflected wave.

In the next sections, we apply the theory and the numerical modeling to a water-steel interface. The associated reflection coefficient have been measured experimentally by Becker and Richardson (1970). Their ultrasonic experiments were verified with an anelastic model in a later paper (Becker and Richardson, 1972) — in particular, the Rayleigh window that cannot be predicted by using reflection coefficients based on the elasticity theory. The isotropic case has been investigated by Borcherdt et al. (1986), who find the Rayleigh window should be observable in appropriate sets of wide-angle reflection data and is useful for estimating the shear-wave quality factor of the ocean bottom. Finally, the theory is used for computing the reflection coefficients of stiff and soft ocean bottoms for various values of δ.

Water-steel interface

The properties of water are $v_f = 1490$ m/s, $\rho = 1000$ kg/m^3, and $Q = 10,000$ at $f_0 = 10$ kHz ($f_0 = 1/2\pi\tau_0$). Steel belongs to the cubic crystal class (e.g., Auld, 1990). The unrelaxed compressional and shear velocities are $v_P = \sqrt{c_{11}/\rho} = \sqrt{c_{33}/\rho} = 5740$ m/s, and $v_S = \sqrt{c_{55}/\rho} = 3142$ m/s, respectively; the density is $\rho = 7932$ kg/m^3; and the dissipation factors at 10 kHz are $Q_1 = 140$ and $Q_2 = 80$. We assume $\delta = 0.5$. The slowness and the wavefront at the high-frequency limit are shown in Figure 2, where one quadrant is displayed.
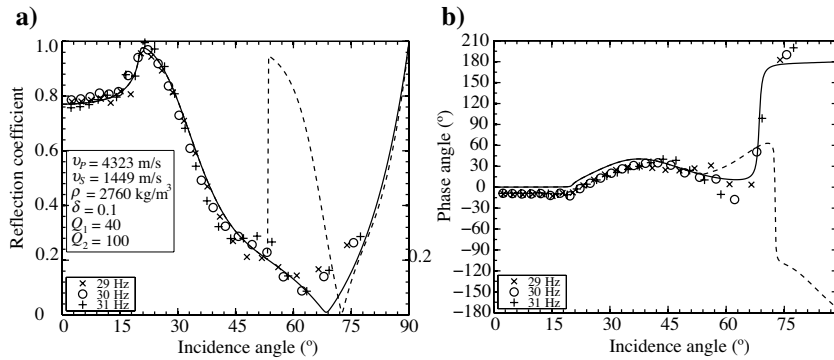

Figure 1. (a) Absolute value and (b) phase angle of the reflection coefficient as a function of the incidence angle. The solid line is the correct coefficient, and the dashed line corresponds to a wrong choice in the sign of the vertical slowness. The symbols represent the numerical calculations applying the AVO method to the synthetic seismograms.
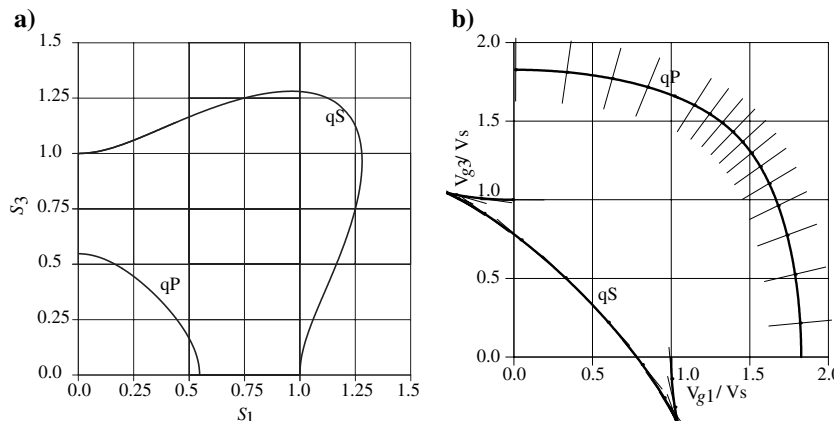

Figure 2. (a) Normalized slownesses and (b) group velocities in steel. The normalization constant is the shear-wave velocity along the Cartesian axes.

Note the cuspidal triangles corresponding to the qS-wave. The thin lines indicate the polarizations.

Figure 3 represents the reflection and transmission coefficients, with the dashed line corresponding to the isotropic and elastic reflection coefficient. Moreover, we perform a numerical evaluation of the reflection coefficient versus incidence angle from the synthetic seismograms. The mesh for the fluid has 375×161 points, and that of the solid has 375×41 points, with both meshes having a horizontal grid spacing of 5 cm; the vertical sizes of the two grids are 3.1 and 1.9 m. The source is a Ricker wavelet located 1.2 m above the interface; it has a dominant frequency of 10 kHz, which is the same as the central frequency of the relaxation peaks. The time step of the Runge-Kutta method is 25 μs. The symbols in Figure 3 correspond to the numerical evaluation of the reflection coefficient.

The perfect agreement between analytical and numerical results emphasize the accuracy of the modeling method.

Ocean bottom

We now consider stiff and soft ocean bottoms. The parameters of the meshes are the same as those used to simulate the case of Figure 1; the only difference is that the mesh for the soft ocean bottom has 121 vertical grid points. The source has a central frequency of 35 Hz and is located 138 m above the interface. The time step of the Runge-Kutta method is 50 μs for the stiff ocean bottom and 25 μs for the soft ocean bottom.

Figure 4 compares the analytical and numerical reflection coefficients for a stiff bottom and various values of δ (indicated in the figure), where $v_P = 4000$ m/s, $v_S = 1920$ m/s, $\epsilon = 0.1$, $\rho = 2460$ kg/m³, $Q_1 = 60$, and $Q_2 = 30$. The equivalent curves for a soft bottom and various values of δ (indicated in the figure) are shown in Figure 5, where $v_P = 1800$ m/s, $v_S = 450$ m/s, $\epsilon = 0$, $\rho = 1600$ kg/m³, $Q_1 = 4$, and $Q_2 = 4$. As can be seen, the change in the reflec-

Figure 3. The Rayleigh window for a water-steel interface. (a) P-wave reflection coefficient and (b) phase angle versus incidence angle. The dashed line corresponds to the isotropic and elastic case, and the symbols correspond to the numerical evaluation of the AVO response.
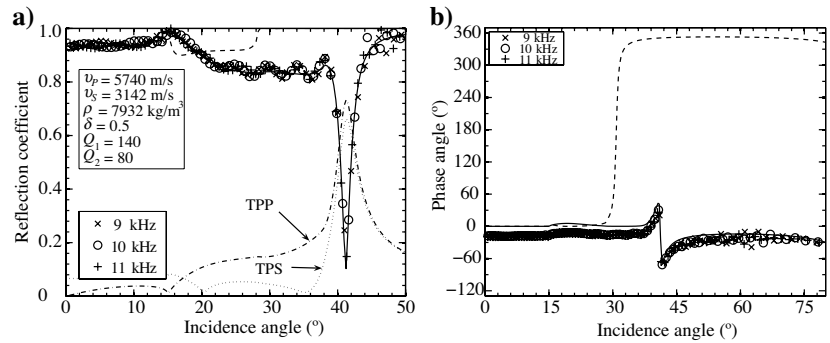

Figure 4. (a) P-wave reflection coefficient and (b) phase angle versus incidence angle for a stiff ocean bottom. The symbols correspond to the numerical evaluation of the AVO response. Curves for various values of δ are shown.
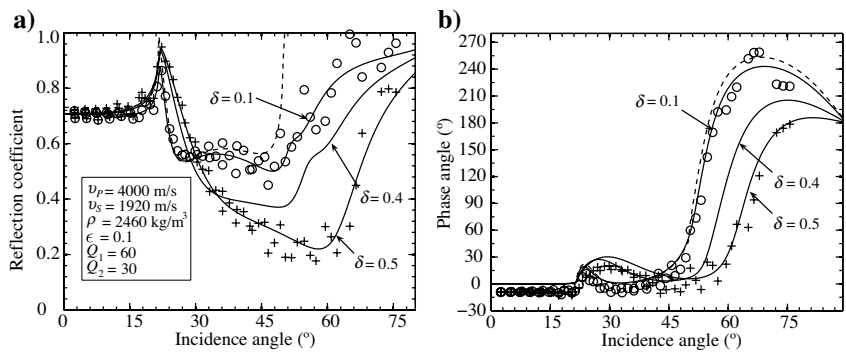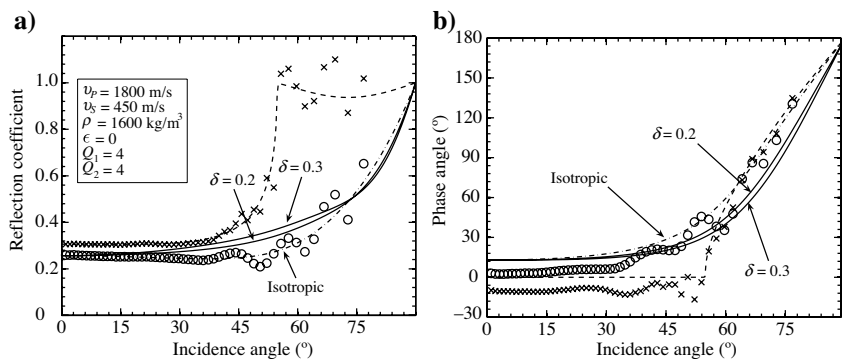

Figure 5. (a) P-wave reflection coefficient and (b) phase angle versus incidence angle for a soft ocean bottom. Curves for various values of δ are shown. The dashed line is the isotropic and elastic case.

tion coefficient is not significant. This means that an AVO analysis cannot discriminate the value of δ.

Figure 6 shows the curves for $\delta = 0.1$, $\epsilon = 0.3$ (lower curve) and for $\delta = 0$, $\epsilon = 0$ (upper curve; the dashed line is the isotropic and elastic case). In this case, the reflection coefficients are dissimilar enough to allow the AVO algorithm to distinguish the two values of ϵ.

Let us consider the Rayleigh window for three values of δ and $\epsilon = 0$. Figure 7 shows the reflection coefficient for the oceanic crust defined by $v_P = 4850$ m/s, $v_S = 2800$ m/s, $\rho = 2600$ kg/m³, $Q_1 = 1000$, and $Q_2 = 10$. As can be seen, the modeling algorithm accurately stimulates the Rayleigh window, i.e., the magnitude of the reflection coefficient and the phase angle. With increasing δ, the win-

dow is shifted toward larger incident angles. If we set $\delta = 0$ and vary ϵ, we obtain the curves displayed in Figure 8. Curves A and B correspond to changes in c_{33} and c_{11}, respectively, with respect to $\epsilon = 0.5$. In this case, the location of the window does not change significantly, but there is a big difference regarding the phases.

The modeling algorithm allows us to model heterogeneous models, such as a stratified ocean bottom and lateral variations of the material properties. Moreover, using generalized coordinates (e.g., Carcione, 1994), ocean-bottom topography can be modeled. In the case of stratified media, more general algorithms are needed to obtain the reflection coefficient from the seismograms. Possible approaches are given by Schoenberg (1978) and Frisk et al. (1980), which could be generalized to the anisotropic case.
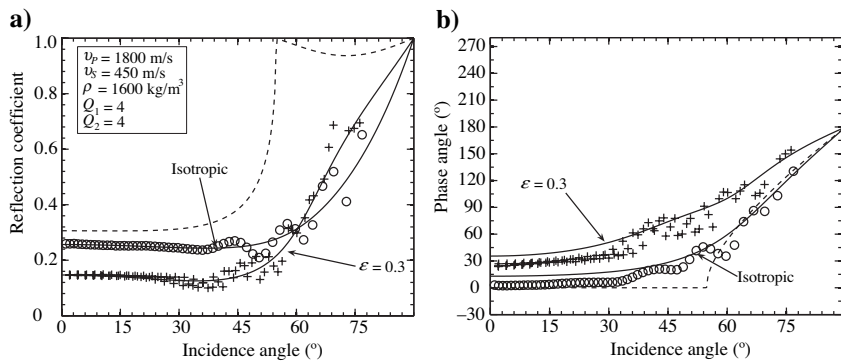

Figure 6. (a) P-wave reflection coefficient and (b) phase angle versus incidence angle. The curves correspond to $\delta = 0.1$, $\epsilon = 0.3$ (lower curve), and $\delta = 0$, $\epsilon = 0$ (upper curve). The dashed line is the isotropic and elastic case, and the symbols represent the numerical evaluation of the AVO response.
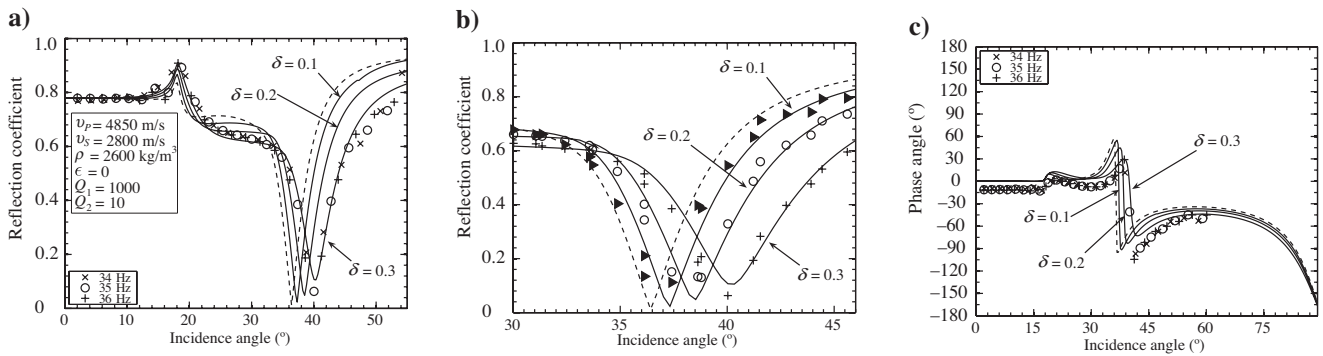

Figure 7. The Rayleigh window for a stiff ocean bottom and various values of δ. (a, b) P-wave reflection coefficient and (c) phase angle versus incidence angle. The dashed line is the isotropic case, and the symbols represent the numerical evaluation of the AVO response.
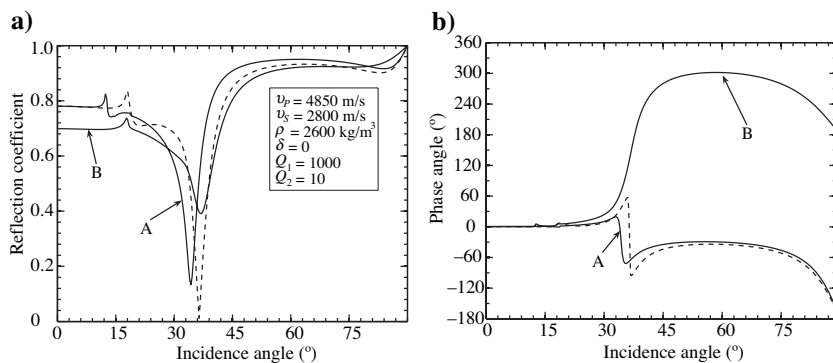

Figure 8. The Rayleigh window for a stiff ocean bottom. (a) P-wave reflection coefficient and (b) phase angle versus incidence angle. Curve A — $\epsilon = 0$, $\epsilon = 0.5$, $c_{33} = \rho v_P^2/(1 + 2\epsilon)$, Curve B — $\epsilon = 0.5$, $c_{11} = (1 + 2\epsilon)\rho v_P^2$. The dashed line is the isotropic case.

CONCLUSIONS

We have analyzed and simulated the seismic reflection of the ocean bottom for an anisotropic-anelastic formation. To our knowledge, the reflection problem, i.e., the calculation of plane-wave reflection coefficients and the numerical simulation in the anisotropic-anelastic case, has not been addressed before. Special attention is given to modeling the boundary conditions at the fluid-solid interface. This is performed accurately by using pseudospectral differential operators and a domain-decomposition method, adapted for fluid/anelastic-anisotropic-solid interfaces.

Changes in δ have no significant effect on the reflection coefficients of a soft ocean bottom. In contrast, they are more sensitive to changes in ϵ. On the other hand, the location of the Rayleigh window, which is observed in stiff bottoms, is sensitive to changes in δ.

The cross-check between the plane-wave analysis and the modeling algorithm confirms the accuracy of both methods and provides an accurate tool for a correct characterization of the ocean-bottom interface. The cross-check is also necessary to test the modeling algorithm because there is no known transient analytical solution in the lossy anisotropic case.

One of the features of the analysis is that nonphysical discontinuities may arise from a wrong chosen sign of the vertical slowness when computing the reflection coefficient. The cross-check with the modeling algorithm allows us to identify this problem and ensure a correct physical analysis of the ocean-bottom reflection event.

ACKNOWLEDGMENTS

APPENDIX A

FREQUENCY-DOMAIN STRESS-STRAIN RELATION

Transforming the memory variable equations 10–12 to the (frequency) ω-domain (e.g., $\partial_t e_1 \rightarrow i\omega e_1$) and substituting the memory variables into equations 6–8, we obtain the stress-strain relation:

$$i\omega \begin{pmatrix} \sigma_{xx} \\ \sigma_{zz} \\ \sigma_{xz} \end{pmatrix} = \begin{pmatrix} p_{11} & p_{13} & 0 \\ p_{13} & p_{33} & 0 \\ 0 & 0 & p_{55} \end{pmatrix} \begin{pmatrix} \partial_x v_x \\ \partial_z v_z \\ \partial_z v_x + \partial_x v_z \end{pmatrix}, \quad \text{(A-1)}$$

where

$$p_{11} = c_{11} - \bar{\mathcal{E}} + \bar{\mathcal{K}} M_1 + c_{55} M_2$$

$$p_{33} = c_{33} - \bar{\mathcal{E}} + \bar{\mathcal{K}} M_1 + c_{55} M_2$$

$$p_{13} = c_{13} - \bar{\mathcal{E}} + \bar{\mathcal{K}} M_1 + c_{55}(2 - M_2)$$

$$p_{55} = c_{55} M_2 \qquad \text{(A-2)}$$

are the complex stiffnesses and

$$M_\nu = \frac{\tau_\sigma^{(\nu)}}{\tau_\epsilon^{(\nu)}} \left(\frac{1 + i\omega \tau_\epsilon^{(\nu)}}{1 + i\omega \tau_\sigma^{(\nu)}} \right), \quad \nu = 1, 2 \qquad \text{(A-3)}$$

are the Zener complex moduli (Zener, 1948; Carcione, 2001). Note that when $\omega \rightarrow \infty$, $p_{IJ} \rightarrow c_{IJ}$.

The relaxation times can be expressed as

$$\tau_\epsilon^{(\nu)} = \frac{\tau_0}{Q_\nu}(\sqrt{Q_\nu^2 + 1} + 1) \quad \text{and} \quad \tau_\sigma^{(\nu)} = \frac{\tau_0}{Q_\nu}(\sqrt{Q_\nu^2 + 1} - 1),$$

$$\text{(A-4)}$$

where τ_0 is a relaxation time such that $1/\tau_0$ is the center frequency of the relaxation peak and Q_ν are the minimum quality factors.

REFERENCES

Auld, B. A., 1990, Acoustic fields and waves in solids: Krieger Publishing Company.
Becker, F. L., and R. L. Richardson, 1970, Ultrasonic critical angle reflectivity, *in* R. S. Sharpe, ed., Research techniques in nondestructive testing: Academic Press Inc., 91–131.
———, 1972, Influence of material properties on Rayleigh critical-angle reflectivity: Journal of the Acoustical Society of America, **51**, 1609–1617.
Borcherdt, R. D., G. Glassmoyer, and L. Wennerberg, 1986, Influence of welded boundaries in anelastic media on energy flow, and characteristics of *P*, *S*-I and *S*-II waves: Observational evidence for inhomogeneous body waves in low-loss solids: Journal of Geophysical Research, **91**, 11503–11118.
Brekhovskikh, L. M., 1960, Waves in layered media: Academic Press Inc.
Carcione, J. M., 1994, The wave equation in generalized coordinates: Geophysics, **59**, 1911–1919.
———, 1998, Scattering of elastic waves by a plane crack of finite width in a transversely isotropic medium: International Journal for Numerical and Analytical Methods in Geomechanics, **22**, 263–275.
———, 2001, Wave fields in real media: Theory and numerical simulation of wave propagation in anisotropic, anelastic and porous media: Pergamon Press.
———, 2006, Vector attenuation: Elliptical polarization and raypaths: Geophysical Prospecting, **54**, 399–407.
Carcione, J. M., and H. B. Helle, 2004, On the physics and simulation of wave propagation at the ocean bottom: Geophysics, **69**, 825–839.
Denneman, A. I. M., G. G. Drijkoningen, D. M. J. Smeulders, and K. Wapenaar, 2002, Reflection and transmission of waves at a fluid/porous-medium interface: Geophysics, **67**, 282–291.
Frisk, G. V., A. V. Oppenheim, and D. R. Martinez, 1980, A technique for measuring the plane-wave reflection coefficient of the ocean bottom: Journal of the Acoustical Society of America, **66**, 606–612.
Krebes, E. S., 1984, On the reflection and transmission of viscoelastic waves — Some numerical results: Geophysics, **49**, 1374–1380.
Postma, G. W., 1955, Wave propagation in a stratified medium: Geophysics, **20**, 780–806.
Richards, P. G., 1984, On wave fronts and interfaces in anelastic media: Bulletin of the Seismological Society of America, **74**, 2157–2165.
Ruud, B. O., 2006, Ambiguous reflections coefficients for anelastic media: Studia Geophysica et Geodaetica, **30**, 479–498.
Santos, J., J. Corbero, C. Ravazzoli, and J. Hensley, 1992, Reflection and transmission coefficients in fluid-saturated porous media: Journal of the Acoustical Society of America, **91**, 1911–1923.
Schoenberg, M., 1978, Nonparametric estimation of the ocean bottom reflection coefficient: Journal of the Acoustical Society of America, **64**, 1165–1170.
Thomsen, L., 1986, Weak elastic anisotropy: Geophysics, **51**, 1954–1966.
Tsvankin, I., 2005, Seismic signatures and analysis of reflection data in anisotropic media: Elsevier Science Publ. Co.
Wu, K., Q. Xue, and L. Adler, 1990, Reflection and transmission of elastic waves from a fluid-saturated porous solid boundary: Journal of the Acoustical Society of America, **87**, 2349–2358.
Zener, C., 1948, Elasticity and anelasticity of metals: University of Chicago Press.